


SCIENTIFIC REPORTS



OPEN

All-laser-micromachining of ridge waveguides in LiNbO₃ crystal for mid-infrared band applications

Lingqi Li¹, Weijie Nie¹, Ziqi Li¹ , Qingming Lu², Carolina Romero³, Javier R. Vázquez de Aldana³ & Feng Chen¹

The femtosecond laser micromachining of transparent optical materials offers a powerful and feasible solution to fabricate versatile photonic components towards diverse applications. In this work, we report on a new design and fabrication of ridge waveguides in LiNbO₃ crystal operating at the mid-infrared (MIR) band by all-femtosecond-laser microfabrication. The ridges consist of laser-ablated sidewalls and laser-written bottom low-index cladding tracks, which are constructed for horizontal and longitudinal light confinement, respectively. The ridge waveguides are found to support good guidance at wavelength of 4 μm. By applying this configuration, Y-branch waveguiding structures (1 × 2 beam splitters) have been produced, which reach splitting ratios of ~1:1 at 4 μm. This work paves a simple and feasible way to construct novel ridge waveguide devices in dielectrics through all-femtosecond-laser micro-processing.

As the basic components in integrated photonics, optical waveguides could confine light propagation within small volumes with dimensions of micrometric or sub-micrometric scales, in which higher optical intra-cavity intensities could be achieved compared with bulk materials¹. Therefore, enhanced optical properties, e.g., lasing performances and nonlinear responses^{2–4}, could be realized in optical waveguides. Particularly, compared with planar waveguide, the ridge waveguides with advantage of stronger spatial confinement of light propagation are particularly desirable for the construction of intricate photonic devices⁵. As a result, some performances of ridge waveguides are intriguing, such as the enhanced efficiency of nonlinear devices^{3,6} and reduced thresholds in integrated lasers⁷. Additionally, the Y-branch waveguides, an essential element for beam splitting or interferometers, has been widely used for electro-optical modulations, optical communications, or integrated optical chips^{8,9}. In addition to silicon, transparent dielectrics are also favorite medium for waveguide devices. Various techniques have been utilized to fabricate diverse guiding structures in transparent optical materials^{10,11}. Generally, in order to fabricate the 2D ridge waveguides, it is required ridge construction on base of planar waveguide layer. For example, in dielectric crystals, a planar waveguide may be formed by ion irradiation or ion implantation in the first step, and second processing with other techniques, such as wet or dry etching, ion-beam enhanced etching, diamond blade dicing, and laser ablation, on the planar waveguide may be implemented to remove the selected parts of the planar waveguide surface, thus constructing the ridge waveguides^{12–16}. Nevertheless, these traditional fabrication solutions require combination of at least two-step processing of diverse techniques. In practice, more convenient and flexible fabrication method of ridge waveguide is desired.

Different from previous works, the ridge structure in this work is fully fabricated by femtosecond (fs) laser micromachining without the combination of other methods. Femtosecond laser micromachining, as one of the most efficient methods, has been widely applied to implement three-dimensional one-step micro-processing in diverse transparent materials for a great variety of applications^{17–22} since the pioneering work by Davis *et al.* in 1996²³. During the processing of fs-laser inscription, the high intensity femtosecond laser is focused at a sample spot at certain depth, resulting in a localized micro-modification of the materials with a refractive index change (negative or positive) through nonlinear absorption processes followed by strong-field ionization and avalanche ionization²⁴. In the dielectric crystals, the femtosecond laser pulses usually induce negative changes ($\Delta n < 0$) of the refractive index due to the localized lattice expansion at the focusing volume (i.e., inside the laser-induced tracks),

¹School of Physics, State Key Laboratory of Crystal Materials, Shandong University, Jinan, 250100, China. ²School of Chemistry and Chemical Engineering, Shandong University, Jinan, 250100, China. ³Grupo de Investigación en Aplicaciones del Láser y Fotónica, Departamento de Física Aplicada, University of Salamanca, Salamanca, 37008, Spain. Correspondence and requests for materials should be addressed to F.C. (email: drfchen@sdu.edu.cn)

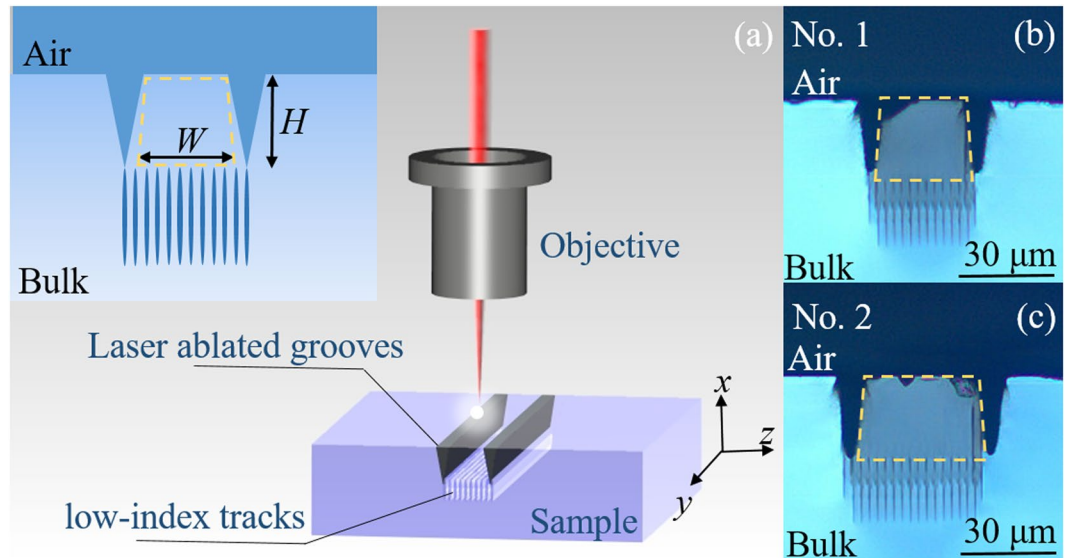


Figure 1. The fabrication of ridge waveguides. (a) Schematic plot of the fabrication process with the femtosecond laser. The inset picture is the schematic diagram of the ridge configuration. Optical microscope image of the cross section of ridge waveguides No. 1. (b) (top) and No. 2 (c) (bottom). The yellow dashed frames indicate the spatial locations of the ridges.

which could be used as low index cladding for waveguide formation (the waveguide cores locate in the regions surrounded by these tracks of $\Delta n < 0$ or regions between the tracks due to the stress-induced effect)^{25,26}. The high intensity pulses of fs-lasers not only produce material damage in the focal volume or surroundings, but can be also used to etch crystals in selected regions through the ultrafast ablation mechanism (Coulomb explosion)^{7,27}. In this work, the novel ridge waveguides are fabricated via all-laser-micromachining: the waveguide core is with lateral confinement of laser-ablated grooves and longitudinal restriction of laser-written bottom low-index cladding tracks. Compared to the ordinary ridge waveguide based on planar waveguide, the fabrication of this geometry of ridge waveguides has shown the superiority of laser-micromachining, such as wide applicability of materials, negligible effect of thermal-diffusion, and ability for maskless 3D processing¹⁸.

The mid-infrared (MIR), typically ranging from 2.5 to 10 μm wavelength, is a strategically important spectral band for a number of applications such as biochemical detection, environmental monitoring, and free-space communication²⁸. As one of the widely used multifunctional crystals, lithium niobate (LiNbO_3) is an ideal candidate due to its unique combination of superior properties such as electro-optic, acousto-optic and piezoelectric properties^{29–31}. Particularly, the transparency of LiNbO_3 crystals ranges from 420 nm to 5200 nm, covering bands from violet till MIR regime. Recently, the LiNbO_3 crystal has attracted tremendous investigations in MIR band applications^{32–34}. Benefiting from the above mentioned advantages, the LiNbO_3 crystal is promising to achieve efficient combination of excellent nonlinear bulk performance and the ridge structures in MIR band. So far, femtosecond-laser micromachined waveguides of Type I direct-write waveguides, Type II stress-induced waveguides^{35–38}, and depressed cladding waveguides geometries²⁵ have been realized in LiNbO_3 crystals. However, ridge waveguides in LiNbO_3 crystal via all-laser-micromachining and their applications to the MIR regime have not been reported. In this work, the novel ridge waveguide and Y-branch structures have been achieved in LiNbO_3 crystal via all-laser-micromachining, which pave a promising way for a wide variety of applications in many disciplines. The guiding properties at MIR wavelength of 4 μm has been measured and discussed in detail. Our work demonstrated a flexible and convenient manner to construct novel ridge geometries in dielectrics via all-femtosecond-laser micro-processing for photonic applications.

Results

The novel ridge waveguides in LiNbO_3 crystal are fabricated by all-laser-micromachining technique. Figure 1(a) depicts the process of the femtosecond laser micromachining. Focused fs-laser pulse produces localized modification in the focal volume forming the laser-written low-index cladding tracks and laser-ablated grooves, which depends on the parameters of the applied fs-laser pulse such as pulsed energy, repetition rate, pulse duration, scanning speed and beam polarization. The inset picture of Fig. 1(a) is the schematic diagram of the ridge configuration, W denotes the bottom-width of the ridges, and $H \sim 25 \mu\text{m}$ is the ablated depth. Figure 1(b) and (c) demonstrate the optical microscope images of the cross-sectional of ridge waveguides No. 1 ($W = 30 \mu\text{m}$) and No. 2 ($W = 50 \mu\text{m}$), in which the ridge outlines can be seen clearly. The core of ridges, as identified by the yellow dashed frame, is located in the regions surrounded by the fs-laser inscribed tracks and fs-laser ablated grooves.

To experimentally investigate the guiding properties of the ridge waveguides along 10-mm-long y -axis at MIR band, an end-face coupling arrangement at wavelength of 4 μm with a linearly polarized laser is employed. Figure 2(a)–(d) illustrate the measured near-field intensity distribution of the waveguides No. 1 and No. 2 along n_o and n_e polarizations at wavelength of 4 μm , respectively. As one can see, both waveguides (No. 1 and No. 2) have

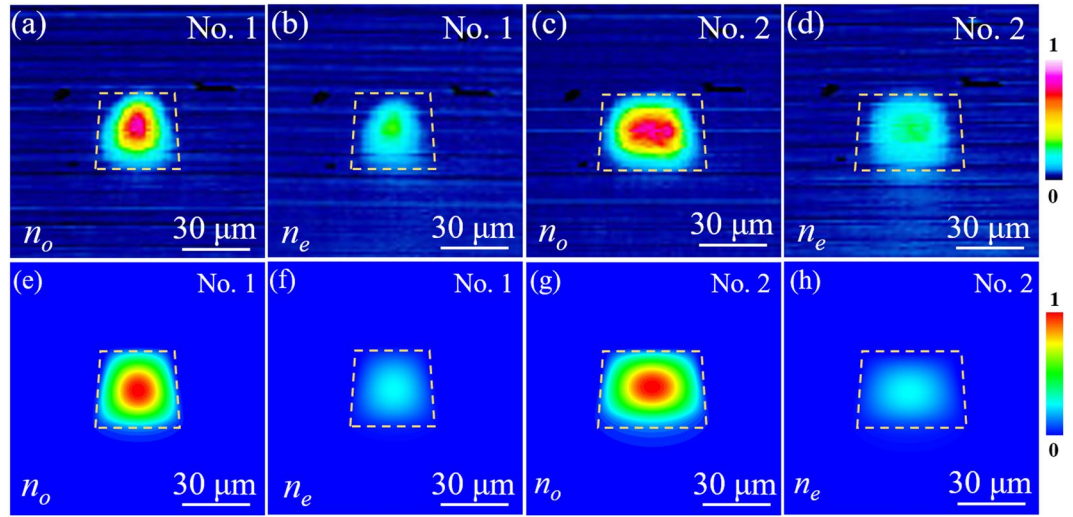


Figure 2. Guiding properties of ridge waveguides. Measured near-field modal distributions of LiNbO₃ ridge waveguides at 4 μm. (a) and (b) No. 1, (c) and (d) No. 2, along n_o (left) and n_e (right) polarization. Calculated near-field modal distributions (e) and (f) No. 1, (g) and (h) No. 2, along n_o (left) and n_e (right) polarization at 4 μm.

shown better guidance along the n_o polarization at MIR wavelength range than those along the n_e polarization, which is in good agreement with the depressed cladding waveguides in LiNbO₃ crystal produced by femtosecond laser micromachining²⁵.

In addition, we calculate the modal profiles of the waveguides numerically based on the estimation of the laser-induced refractive index changes. By assuming a step-index profile, the maximum refractive index modification between the waveguide core and substrate can be roughly estimated with the Eq. 1

$$\Delta n_{o,e} \approx \frac{\sin^2 \theta_m}{2n_{o,e}} \quad (1)$$

where θ_m is the maximum incident angular deflection at which no change of the transmitted power occurred, n_o and n_e are the refractive index of LiNbO₃ at 4 μm. In this work, the calculated maximum refractive index change for waveguides No. 1 and No. 2 at 4 μm are 4.8×10^{-3} and 5.2×10^{-3} along the n_o polarization, respectively. However, the values of the n_e polarization are 1.3×10^{-3} and 2.1×10^{-3} , which are much smaller than those along the n_o polarization. The smaller refractive index alternations along the n_e polarization may also cause larger propagation loss along the n_e polarization. With the obtained refractive index changes, the spatial distributions of the index have been reconstructed (Fig. 3(a) (n_o) and Fig. 3(b) (n_e)). According to these 2D refractive index profiles, the near-field intensity profiles are simulated by the FD-BPM algorithm (Rsoft[®] Beam PROP)³⁹, which is based on the finite difference beam propagation method (FD-BPM)⁴⁰. Figure 2(e)–(f) illustrate the calculated modal distributions of the waveguides along both n_o and n_e polarizations at 4 μm, showing a good accordance with the experimental data.

Based on the end-face coupling arrangement, the propagation losses of the ridge waveguide of LiNbO₃ were measured. The propagation loss can be calculated by using the Eq. 2⁴¹:

$$\alpha = \frac{-10}{L} \log_{10} \left[\frac{P_{out}}{\eta P_{in} (1 - R)^2} \right] \quad (2)$$

where P_{in} is the in-coupled light power and P_{out} is the output light power. The length of light propagating in the sample is written as L . R is the reflectance, and we calculate $R_o \sim 0.87$ and $R_e \sim 0.89$ at 4 μm. Considering the mismatch coefficient η which can be calculated by an overlap integral between both the launched Gaussian field profiles and the modal profiles of the structure. The mismatch coefficient η can be expressed as^{42,43}

$$\eta = \int \phi_m^*(x) \phi(x, z) dx \quad (3)$$

where $\phi_{in}(x) = \sum_m c_m \phi_m(x)$ is the incident field, which is assumed as the Gaussian field. $\phi(x, z) = \sum_m c_m \phi_m(x) e^{i\beta z}$ is the propagating modal profiles of the structure and β is the propagation constant. The values of the mismatch coefficient have been calculated by FD-BPM algorithm (Rsoft[®] Beam PROP), which are ~ 0.53 and 0.47 for waveguides No. 1 and No. 2, respectively. Finally, we can approximately calculate the propagation losses (listed in Table 1.) of the ridge waveguides in LiNbO₃. The higher attenuation for ridge waveguide should be partly attributed to the non-perfect side-walls fabricated by the fs-laser. It is clearly that the propagation loss decreases with the increase of the width of ridge waveguides from 30 μm to 50 μm. The phenomenon, we believe, is caused by the

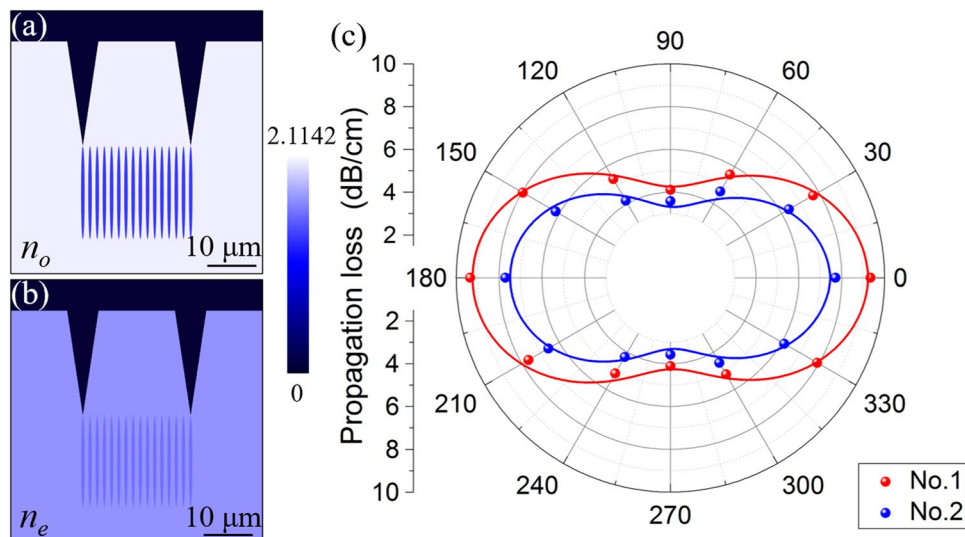


Figure 3. Reconstructed refractive index profile and polarization properties of ridge waveguides. Reconstructed refractive index profile of n_o (a) and n_e (b) of No.1. (c) Polarization images of the propagation loss of ridges No. 1 and No. 2 at $4\mu\text{m}$.

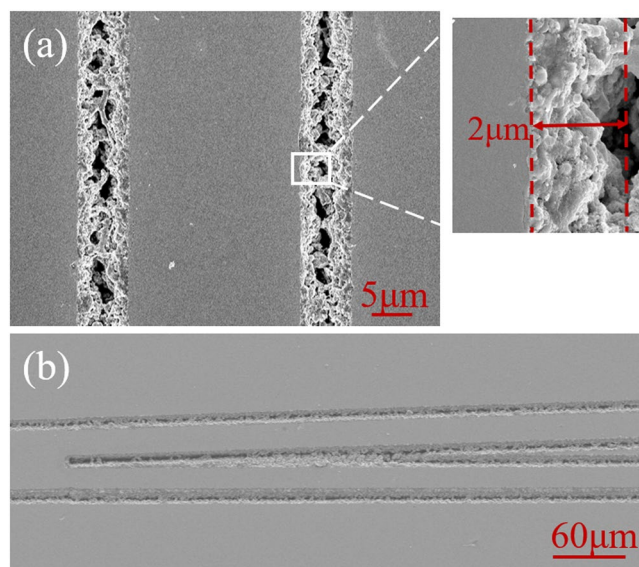


Figure 4. The topographic SEM image of ridge waveguides. (a) The SEM image of the ridge waveguide surface. The inset picture show the sidewalls of ridge waveguide. (b) The SEM image of the intersection of Y-branch.

	No. 1	No. 2	Y-branch
n_o	4.61	3.58	4.28
n_e	9.35	7.71	12.09

Table 1. Propagation losses α (dB/cm) of the LiNbO_3 ridge waveguides at $4\mu\text{m}$.

lateral roughness of the ridges and the rough sidewalls affect the light propagation more strongly for narrower waveguide. In order to estimate the roughness of the sidewalls, we used scanning electron microscopy (SEM) to obtain the surface topographic image of the ridge waveguide (see Fig. 4(a)). As one can see, the roughness is estimated to be $\sim 2.0\mu\text{m}$ as the insert shows. One can expect the reduction of the roughness of the side walls by using post-ablation treatment (such as ion-beam sputtering)⁴⁴, multiscan (instead of single-scan) of fs-laser ablation⁴⁵ and wet etching⁴⁶, which will reduce the propagation losses to a certain extent. In order to achieve thorough information of the polarization effects for propagating properties, the all-angle light transmission along the transverse plane has been measured in waveguides No. 1 and No. 2, as shown in Fig. 3(c). The minimum propagation loss

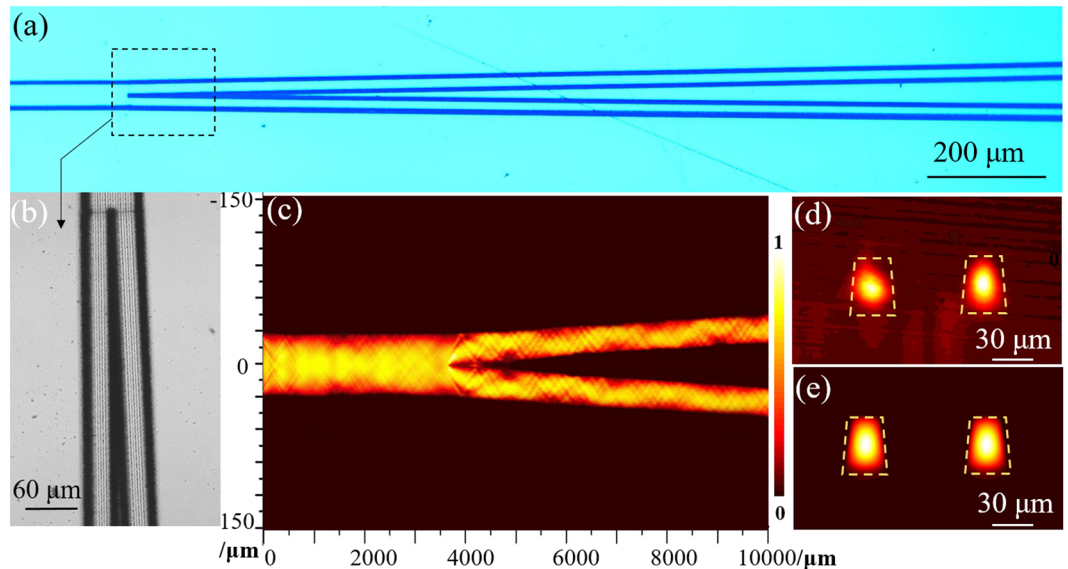


Figure 5. Optical microscope image and guiding properties of Y-branch waveguides. (a) The optical microscope image of the top view of the Y-branch. (b) The optical microscope image of the splitting point of the Y-branch. (c) The top view of simulated light propagating on the YZ-plane at $4\mu\text{m}$. (d) Measured modal profile of the cross-section of Y-branch at $4\mu\text{m}$. (e) Simulated modal profile of the cross-section of Y-branch at $4\mu\text{m}$.

appears when polarization angles are 90° and 270° , which is along the n_o polarization. The maximum propagation loss occurs when polarization angles are 0° and 180° (n_e polarization).

By applying this novel ridge configuration, Y-branch structure (1×2 beam splitters) has successfully produced. The Y-branch structure waveguide is designed with a straight 3.8 mm length input arm ($60\mu\text{m}$ width), and two output arms ($30\mu\text{m}$ width) with the divergence of 0.46° , which corresponds to the lateral separation of $50\mu\text{m}$. Figure 5(a) depicts the top view of the Y-branch waveguide, the splitting point of the Y-branch structure can be clearly seen in Fig. 5(b), the darker line around splitting point is produced by the irradiation with a larger amount of pulses as it is a stopping and starting point for the stage motion. Figure 4(b) exhibits the topographic SEM images of the intersection of Y-branch structure. As expected, the good guiding performance along n_o polarization of the straight waveguides has also been found in the Y-branch splitter (Fig. 5(d)). Based on the calculated maximum refractive index change of 5.0×10^{-3} along n_o polarization, the near-field intensity profiles have been simulated. Figure 5(c) shows the top view of simulated light propagating on the YZ-plane at $4\mu\text{m}$. Moreover, the simulated Y-branch cross-sectional modal profile at $4\mu\text{m}$ has also been depicted in Fig. 5(e), which is in good agreement with the experimental results (Fig. 5(d)). In addition, the propagation loss of the Y-branch is 4.28 dB/cm along n_o polarization at $4\mu\text{m}$. Particularly, the measured output splitting ratio for the two arms is 1:1.12, showing the excellent performance for the Y-branch splitter function.

Discussion

The ridge structures consisting of laser-ablated sidewalls and laser-written bottom low-index cladding tracks have been designed and fabricated by in a LiNbO_3 crystal wafer. The configuration of laser-ablated grooves and laser-written low-index tracks has been demonstrated to be an efficient way to build compact structures capable of efficient beam profile manipulation, including basic functions of beam splitting. In this work, the ridge waveguide and Y-branch structure have been achieved and implemented to the MIR regime in LiNbO_3 crystal via all-laser-micromachining, which pave a promising way for a wide variety of applications in many disciplines. On the one hand, from the perspective of fabrication, our work shows the capability of fs-laser micro-fabrication to produce more complex waveguiding devices by integration of more designable elements in a single crystal chip, which would further enlarge the scope of promising applications related to this fabrication technique. Additionally, unlike the ordinary ridge waveguide based on planar waveguide, this technique has demonstrated the superiority of laser-micromachining, e.g., direct, rapid and mask-free features. On the other hand, by applying this ridge configuration, Y-branch structure (1×2 beam splitters) has successfully produced. The novel ridge structure in LiNbO_3 with the lateral confinement of laser-ablation grooves and longitudinal restriction of laser-written low-index cladding tracks could be used for a wide variety of applications, such as electro-optical modulator, signal amplification, and frequency conversion. Finally, the exploration on the improvement of the sidewall quality to reduce the roughness is required in future work, which may be achieved by combining the suitable wet-etching (e.g., by HF acid). And one could extend this technique in other crystals to obtain waveguide devices for broader-scope applications of both scientific researches and human life. In conclusion, our work demonstrates a new ridge configuration by employing the all-laser-micromachining. Based on the new ridge waveguide, Y-branch structure has been implemented. This work paves a way to produce nonlinear optical devices for light guiding, beam splitting in dielectrics for various photonic applications at MIR regime.

Methods

Fabrication of ridge waveguides. The x -cut LiNbO₃ crystal sample used in this work was cut into wafers with dimensions of $2 \times 10 \times 10 \text{ mm}^3$ ($x \times y \times z$) and optically polished. To obtain the novel ridge waveguides and Y-splitters, a Ti:Sapphire amplified laser system (Spitfire, Spectra Physics) was utilized, in which linearly polarized pulses (120 fs duration, 796 nm central wavelength, 1 mJ maximum energy, and 1 kHz repetition rate) was delivered. In the first step to fabricate the low-index cladding tracks, the laser beam was focused at $20 \mu\text{m}$ below the largest surface ($8 \text{ mm} \times 10 \text{ mm}$) by a $40 \times$ microscope objective (N.A. = 0.65) with a pulse energy of $\sim 0.32 \mu\text{J}$. The sample, located at a three-dimensional motorized stage with a spatial resolution of $0.2 \mu\text{m}$. While the sample was scanned at a constant velocity of $500 \mu\text{m/s}$ along the 10-mm edge, a damage line was produced inside the sample. The procedure was repeated and several parallel low-index cladding tracks ($3\text{-}\mu\text{m}$ lateral separation of adjacent parallel tracks) were inscribed at same depth of the sample, producing the longitudinal confinement of light propagation. Secondly, in order to get ablation grooves with depth of $\sim 20 \mu\text{m}$ and with crater walls as vertical as possible, the laser beam was focused at the surface by a $10 \times$ microscope objective (N.A. = 0.25). A larger pulse energy (four times larger than that on the first step) of $1.2 \mu\text{J}$, was set at a much slower scanning speed of $100 \mu\text{m/s}$. Therefore, an ablation channel was formed. The fabrication procedure was repeated to produce an additional channel with lateral separation (the width of ridges) enough to equal the length of the bottom parallel low-index cladding tracks. With the lateral confinement of ablation grooves and longitudinal restriction of parallel low-index cladding tracks, the 10-mm long novel ridge waveguide was produced on the surface of the LiNbO₃ crystal. The schematic plot of the experimental setup is depicted in Fig. 1(a).

Characterization of Guidance. The cross-sectional microscope images of ridge waveguides were taken by using an optical microscope (Axio Imager, Carl Zeiss) operating in transmission mode. The SEM images were obtained using a field-emission scanning electron microscope (SU8010). The near-field modal distributions were investigated by employing a typical end-face arrangement. The linearly polarized laser (Daylight Solutions, Inc.), was focused with a MIR microscope objective lens (ZnSe, LFO-5-12-3.75, N.A. = 0.13) in one end-face of the waveguides. Afterwards, the modal profile at the output of the waveguide was imaged onto a MIR beam imaging camera (WinCamD, DataRay Inc.) by another same objective lens. Based on the above arrangement, the propagation losses were determined by directly measuring the light powers coupled into and out of the end-faces. The coupling efficiency was estimated by considering the overlap of the incident light beam and waveguide mode. The coupling and Fresnel reflection losses of the waveguide systems were calculated as well.

References

- Kip, D. Photorefractive waveguides in oxide crystals: fabrication, properties, and applications. *Appl. Phys. B* **67**, 131–150 (1998).
- Griivas, C. Optically pumped planar waveguide lasers, Part I: Fundamentals and fabrication techniques. *Prog. Quant. Electron.* **35**, 159 (2011).
- Iwai, M. *et al.* High-power blue generation from a periodically poled MgO: LiNbO₃ ridge-type waveguide by frequency doubling of a diode end-pumped Nd: Y₃Al₅O₁₂ laser. *Appl. Phys. Lett.* **83**, 3659–3661 (2003).
- Kroesen, S., Tekce, K., Imbrock, J. & Denz, C. Monolithic fabrication of quasi phase-matched waveguides by femtosecond laser structuring the $\chi^{(2)}$ nonlinearity. *Appl. Phys. Lett.* **107**, 101109 (2015).
- Chen, F. Construction of two-dimensional waveguides in insulating optical materials by means of ion beam implantation for photonic applications: Fabrication methods and research progress. *Crit. Rev. Solid State Mater. Sci.* **33**, 165–182 (2008).
- Kurimura, S., Kato, Y., Maruyama, M., Usui, Y. & Nakajima, H. Quasi-phase-matched adhered ridge waveguide in LiNbO₃. *Appl. Phys. Lett.* **89**, 191123 (2006).
- Jia, Y. *et al.* Ridge waveguide lasers in Nd:GGG crystals produced by swift carbon ion irradiation and femtosecond laser ablation. *Opt. Express* **20**, 9763–9768 (2012).
- Kondo, T., Matsuo, S., Juodkazis, S. & Misawa, H. Femtosecond laser interference technique with diffractive beam splitter for fabrication of three-dimensional photonic crystals. *Appl. Phys. Lett.* **79**, 725–727 (2001).
- He, R., Hernández-Palmero, R., Romero, C., Vázquez de Aldana, J. R. & Chen, F. Three-dimensional dielectric crystalline waveguide beam splitters in mid-infrared band by direct femtosecond laser writing. *Opt. Express* **22**, 31293–31298 (2014).
- Korkishko, Y. N. *et al.* Reverse proton exchange for buried waveguides in LiNbO₃. *J. Opt. Soc. Am. A* **15**, 1838–1842 (1998).
- Chen, F. Micro- and submicrometric waveguiding structures in optical crystals produced by ion beams for photonic applications. *Laser Photonics Rev.* **6**, 622–640 (2012).
- Hu, H., Ricken, R., Sohler, W. & Wehrspohn, R. B. Lithium niobate ridge waveguides fabricated by wet etching. *IEEE Photonic Technol. Lett.* **19**, 417–419 (2007).
- Hartung, H. *et al.* Fabrication of ridge waveguides in zinc-substituted lithium niobate by means of ion-beam enhanced etching. *Opt. Lett.* **33**, 2320–2322 (2008).
- Takigawa, R., Higurashi, R., Kawanishi, T. & Asano, T. Lithium niobate ridged waveguides with smooth vertical sidewalls fabricated by an ultra-precision cutting method. *Opt. Express* **22**, 27733–27738 (2014).
- Mendivil, J. M. D., Hoyos, J. D., Solís, J. & Lifante, G. Ridge waveguide laser in Nd: LiNbO₃ by Zn-diffusion and femtosecond-laser structuring. *Opt. Mater.* **62**, 353–356 (2016).
- Jia, Y., Tan, Y., Cheng, C., Vázquez de Aldana, J. R. & Chen, F. Efficient lasing in continuous wave and graphene Q-switched regimes from Nd:YAG ridge waveguides produced by combination of swift heavy ion irradiation and femtosecond laser ablation. *Opt. Express* **22**, 12900–12908 (2014).
- Gattass, R. R. & Mazur, E. Femtosecond laser micromachining in transparent materials. *Nature Photon.* **2**, 219–225 (2008).
- Sugioka, K. & Cheng, Y. Ultrafast lasers—reliable tools for advanced materials processing. *Light Sci. Appl.* **3**, e149 (2014).
- Sun, Y.-L. *et al.* Protein-based soft micro-optics fabricated by femtosecond laser direct writing. *Light Sci. Appl.* **3**, e129 (2014).
- Liao, Y. *et al.* High-fidelity visualization of formation of volume nanogratings in porous glass by femtosecond laser irradiation. *Optica* **2**, 329–334 (2015).
- Sugioka, K. *et al.* Femtosecond laser 3D micromachining: a powerful tool for the fabrication of microfluidic, optofluidic, and electrofluidic devices based on glass. *Lab Chip*. **14**, 3447 (2014).
- Choudhury, D., Macdonald, J. R. & Kar, A. K. Ultrafast laser inscription: perspectives on future integrated applications. *Laser Photonics Rev.* **8**, 827 (2014).
- Davis, K. M., Miura, K., Sugimoto, N. & Hirao, K. Writing waveguides in glass with a femtosecond laser. *Opt. Lett.* **21**, 1729–1731 (1996).
- Chen, F. & de Aldana, V. J. R. Optical waveguides in crystalline dielectric materials produced by femtosecond-laser micromachining. *Laser Photonics Rev.* **8**, 251 (2014).

25. He, R. *et al.* Femtosecond laser micromachining of lithium niobate depressed cladding waveguides. *Opt. Mater. Express* **3**, 1378–1384 (2013).
26. Nie, W. *et al.* Dual-wavelength waveguide lasers at 1064 and 1079 nm in Nd:YAP crystal by direct femtosecond laser writing. *Opt. Lett.* **40**, 2437–2440 (2015).
27. Cheng, Y. *et al.* Mid-infrared ridge waveguide in MgO: LiNbO₃ crystal produced by combination of swift O⁵⁺ ion irradiation and precise diamond blade dicing. *Opt. Mater.* **48**, 209–214 (2015).
28. Hu, J., Meyer, J., Richardson, J. & Shah, L. Feature issue introduction: mid-IR photonic materials. *Opt. Mater. Express* **3**, 1571–1575 (2013).
29. Arizmendi, L. Photonic applications of lithium niobate crystals. *Phys. Status Solidi A* **201**, 253–283 (2004).
30. Sohler, W. *et al.* Integrated optical devices in lithium niobate. *Opt. Photonics News* **19**, 24–31 (2008).
31. Jin, H. *et al.* On-chip generation and manipulation of entangled photons based on reconfigurable lithium-niobate waveguide circuits. *Phys. Rev. Lett.* **113**, 103601 (2014).
32. Heese, C., Phillips, C. R., Gallmann, C. R., Fejer, M. & Keller, U. Ultrabroadband, highly flexible amplifier for ultrashort midinfrared laser pulses based on aperiodically poled Mg: LiNbO₃. *Opt. Lett.* **35**, 2340–2342 (2010).
33. Wang, Z. *et al.* High-repetition-rate narrow pulse width mid-infrared optical parametric oscillator based on PPMgLN crystal. *Laser Phys.* **26**, 025401 (2015).
34. Rotermund, F., Petrov, V. & Noack, F. Laser-diode-seeded single and double stage femtosecond optical parametric amplification in the mid-infrared. *Opt. Quant. Electron.* **32**, 1057–1067 (2000).
35. Lv, J., Hao, J. & Chen, F. Green up-conversion and near-infrared luminescence of femtosecond-laser-written waveguides in Er³⁺, MgO co-doped nearly stoichiometric LiNbO₃ crystal. *Opt. Express* **24**, 25482–25490 (2016).
36. Thomas, J. *et al.* Laser direct writing: Enabling monolithic and hybrid integrated solutions on the lithium niobate platform. *Phys. Status Solidi A* **208**, 276–283 (2011).
37. Heinrich, M. *et al.* Evanescent coupling in arrays of type II femtosecond laser-written waveguides in bulk x-cut lithium niobate. *Appl. Phys. Lett.* **93**, 101111 (2008).
38. Qi, J. *et al.* Fabrication of polarization-independent single mode waveguides in lithium niobate crystal with femtosecond laser pulses. *Opt. Mater. Express* **6**, 2554–2559 (2016).
39. Rsoft Design Group. Rsoft: A software for photonic and optical network design, Synopsys' Optical Solutions Group for optical design and analysis, California, USA, <https://optics.synopsys.com/rsoft/> (1994).
40. Yevick, D. & Bardyszewski, W. Correspondence of variational finite-difference (relaxation) and imaginary-distance propagation methods for modal analysis. *Opt. Lett.* **17**, 329–330 (1992).
41. Wang, L. *et al.* Low-loss planar and stripe waveguides in Nd³⁺-doped silicate glass produced by oxygen-ion implantation. *J. Appl. Phys.* **101**, 053112 (2007).
42. Feit, M. D. & Fleck, J. A. Computation of mode properties in optical fiber waveguides by a propagating beam method. *Appl. Opt.* **19**, 1154–1164 (1980).
43. Yevick, D. & Hermansson, B. New Formulations of the Matrix Beam Propagation Method: Application to Rib Waveguides. *IEEE J. Quantum Electron.* **25**, 221–229 (1989).
44. Degl'Innocenti, R. *et al.* Micromachining of ridge optical waveguides on top of He⁺-implanted β-BaB₂O₄ crystals by femtosecond laser ablation. *J. Appl. Phys.* **100**, 113121 (2006).
45. Sun, H. *et al.* Fabrication of microfluidic optical waveguides on glass chips with femtosecond laser pulses. *Opt. Lett.* **32**, 1536–1538 (2007).
46. Li, Q. *et al.* Sapphire-Based Fresnel Zone Plate Fabricated by Femtosecond Laser Direct Writing and Wet Etching. *IEEE Photon. Technol. Lett.* **28**, 1290–1293 (2016).

Acknowledgements

This work was supported by Natural National Science Foundation of China (11274203), Project 111 of China (B13029) and Junta de Castilla y León (Project SA116U13, SA046U16), Spanish Ministerio de Economía y Competitividad (MINECO, FIS2013-44174-P, FIS2015-71933-REDT).

Author Contributions

L.L., W.N., Z.L. and F.C. performed all the experiments and simulation. C.R. and J.R.V.A. produced the ridge waveguides of LiNbO₃ crystal. Q.L. polished the waveguide sample. All the authors discussed the results and participated in the manuscript preparation.

Additional Information

Competing Interests: The authors declare that they have no competing interests.

Publisher's note: Springer Nature remains neutral with regard to jurisdictional claims in published maps and institutional affiliations.



Open Access This article is licensed under a Creative Commons Attribution 4.0 International License, which permits use, sharing, adaptation, distribution and reproduction in any medium or format, as long as you give appropriate credit to the original author(s) and the source, provide a link to the Creative Commons license, and indicate if changes were made. The images or other third party material in this article are included in the article's Creative Commons license, unless indicated otherwise in a credit line to the material. If material is not included in the article's Creative Commons license and your intended use is not permitted by statutory regulation or exceeds the permitted use, you will need to obtain permission directly from the copyright holder. To view a copy of this license, visit <http://creativecommons.org/licenses/by/4.0/>.

© The Author(s) 2017